Research Square

Preprints are preliminary reports that have not undergone peer review.
They should not be considered conclusive, used to inform clinical practice,
or referenced by the media as validated information.

Thermal Stability and Photovoltaic Enhancement of Double Perovskite ($Cs_2InSbCl_6$) Based Solar Cell (p-i-n) through Thickness and Bandgap Optimization

Mouad Chettab

mouad.chettab@doc.umc.edu.dz

Université de Frères Mentouri Constantine 01

Research Article

Keywords: Cs2InSbCl6, SCAPS-1D, Temperature, solar cell, Efficiency

Posted Date: June 26th, 2026

DOI: https://doi.org/10.21203/rs.3.rs-9837443/v1

License: This work is licensed under a Creative Commons Attribution 4.0 International License.
Read Full License

Additional Declarations: No competing interests reported.

Thermal Stability and Photovoltaic Enhancement of Double Perovskite ($Cs_2InSbCl_6$) Based Solar Cell (p-i-n) through Thickness and Bandgap Optimization.

Mouad Chettab[1*]

[1]Thin films and interfaces laboratory, Université de Frères Mentouri Constantine 01, Constantine, Algérie.

mouad.chettab@doc.umc.edu.dz

Correspondent author: **Mouad Chettab**

Abstract

In this work, a comprehensive numerical investigation of the Fe/CuO/$Cs_2InSbCl_6$/CdS/TiO_2 heterostructure solar cell was carried out using the SCAPS-1D simulator under AM1.5G illumination conditions at 300 K. The effects of absorber thickness, bandgap energy, transport layer properties, and operating temperature on the photovoltaic performance were systematically analyzed. Optical analysis revealed that the ($Cs_2InSbCl_6$) absorber exhibits strong visible-light absorption, while the (CdS) and (TiO_2) layers maintain high transparency due to their wide bandgap energies. The optimization study demonstrated that the photovoltaic performance strongly depends on the absorber layer properties. The optimal absorber thickness was found within the range 0.9µm, with an optimal bandgap energy of approximately 1.4 eV. Under optimized conditions, the proposed device achieved a maximum power conversion efficiency (PCE) of nearly 28 %, accompanied by an open-circuit voltage (Voc) approaching 0.98 V, a short-circuit current density exceeding 34 mA/cm^2, and a fill factor (FF) close to 86 %. The ideality factor decreased from approximately 1.8 before optimization to nearly 1.6 after optimization, confirming reduced recombination losses and improved junction quality. In contrast, variations in (CdS) and (TiO_2) thicknesses and bandgap energies produced only slight changes in the photovoltaic parameters, indicating stable band alignment and efficient carrier transport across the heterostructure interfaces. Thermal stability analysis performed between 300 and 350 K revealed a gradual efficiency degradation from nearly 27 to approximately 24 %. The extracted temperature coefficients were approximately -0.22% K^{-1} for (PCE), -2.29 mV.K^{-1} for (V_{oc}), and -0.06 % K^{-1} for (FF), whereas (J_{sc}) exhibited only weak thermal dependence. Overall, the obtained results demonstrate that the proposed Fe/CuO/$Cs_2InSbCl_6$/CdS/TiO_2 architecture possesses excellent photovoltaic performance, reduced recombination losses, and acceptable thermal stability, making it a promising candidate for next-generation high-efficiency perovskite solar cells.

Keywords: $Cs_2InSbCl_6$, SCAPS-1D, Temperature, solar cell, Efficiency.

1. Introduction

The growing global demand for clean and sustainable energy has intensified research efforts toward the development of high-efficiency and environmentally friendly photovoltaic technologies [1]. Among the various emerging photovoltaic materials, perovskite solar cells (PSCs) have attracted tremendous attention owing to their remarkable optoelectronic properties [2], including high absorption coefficients, tunable bandgap energies [3], long carrier diffusion lengths, excellent charge transport characteristics [4] and low exciton binding energy [5]. These outstanding properties have enabled perovskite-based solar cells to achieve rapid improvements in power conversion efficiency (PCE), making them one of the most promising candidates for next-generation photovoltaic applications. Conventional lead-based perovskites have demonstrated exceptional photovoltaic performance; however, their commercialization remains limited due to issues associated with lead toxicity [6], environmental instability, and thermal degradation [7]. Consequently, increasing attention has been directed toward the development of lead-free and thermally stable perovskite materials capable of maintaining high photovoltaic performance while minimizing environmental concerns [8]. Among these materials, double perovskites ($A_2BB"X_6$) have emerged as attractive alternatives [9], because of their enhanced structural stability [10], low toxicity, and favorable electronic properties. Recently, the vacancy-ordered double perovskite ($Cs_2InSbCl_6$) has gained considerable interest as a potential absorber material for photovoltaic

applications. This material exhibits excellent chemical stability, suitable bandgap energy, strong visible-light absorption, and improved resistance against thermal degradation compared with conventional organic-inorganic perovskites. In addition, the inorganic nature of ($Cs_2InSbCl_6$) contributes to enhanced environmental and thermal robustness, which is essential for stable long-term solar cell operation under practical working conditions. Moreover, this solar cell adopts an n-i-p architecture in which the intrinsic absorber layer is based on ($Cs_2InSbCl_6$). In comparison with conventional p-n junction semiconductor devices, the n-i-p structure demonstrates improved sensitivity toward long-wavelength photon absorption [9]. Under illumination, the perovskite generates exciton (electron–hole pairs), which dissociate at the interface, allowing electrons to move toward the (ETL) and holes toward the (HTL), which enhances the built-in electric field and accelerates charge separation at the layer interfaces [11].

The photovoltaic performance of a solar cell strongly depends not only on the absorber layer but also on the transport layers and interfacial properties. Proper band alignment between the absorber, buffer, and carrier transport layers plays a crucial role in reducing recombination losses and improving carrier extraction efficiency. In this context, (CuO) has attracted significant interest as a Hole Transport Layer (HTL) [12],[13] due to its high hole mobility [14], good chemical stability, suitable valence band alignment, and low fabrication cost [15] . Similarly, (CdS) [12] and (TiO_2) [16] are widely employed as buffer and electron transport layers (ETLs), respectively, because of their favorable electronic properties, high transparency, and efficient electron extraction capability. In addition to material selection, the optimization of absorber thickness and bandgap energy is essential for achieving high photovoltaic performance. The absorber thickness directly affects photon absorption capability and carrier transport distance, while the bandgap energy controls the spectral absorption range and open-circuit voltage. Furthermore, operating temperature significantly influences solar cell performance through changes in carrier recombination, saturation current density, and bandgap narrowing effects. Therefore, thermal stability analysis is of major importance for evaluating the reliability and practical applicability of photovoltaic devices. Several studies like [4], [5], [8], [17], [18], [19] have investigated the optimization of perovskite solar cells using numerical simulation tools, particularly the Solar Cell Capacitance Simulator (SCAPS-1D), which provides accurate analysis of carrier transport, recombination mechanisms, and interface effects in multilayer photovoltaic structures. SCAPS-1D solves the Poisson and carrier continuity equations self-consistently using numerical iterative methods, allowing detailed investigation of device physics under different operating conditions [20].

In the present work, a comprehensive numerical investigation of the Fe/CuO/$Cs_2InSbCl_6$/CdS/TiO_2 heterostructure solar cell is carried out using SCAPS-1D simulation software. The study mainly focuses on the thermal stability and temperature-dependent photovoltaic behavior of the proposed device. In addition, the effects of absorber thickness, bandgap energy, and transport layer properties on the photovoltaic performance are systematically analyzed. The electrical characteristics, including current density-voltage (J-V) behavior, capacitance response, ideality factor, and recombination mechanisms, are thoroughly investigated to understand the carrier transport dynamics and thermal degradation behavior of the device. The obtained results aim to provide valuable insights into the optimization of thermally stable and high-efficiency lead-free double perovskite solar cells for future photovoltaic applications.

2. Methodology

2.1. Computational Method in SCAPS-1D.

The numerical modeling in SCAPS-1D is based on the simultaneous solution of Poisson's equation, carrier continuity equations, and transport equations for electrons and holes. These equations describe the electrostatic potential distribution, charge carrier transport, recombination mechanisms, and photogeneration processes inside the multilayer device structure. The electrostatic behavior within the device is governed by [3]:

$$\frac{\partial^2\psi}{\partial x^2} = \frac{-\partial E}{\partial x} = \frac{\rho}{\epsilon_s} = \frac{-q}{\epsilon_s}(p - n + N_d^+ - N_a^- \pm N_{def}) \quad (1)$$

While the electron and hole continuity equations are expressed as [21],[22]:

$$-\frac{\partial J_p}{\partial x}+G-U_P(n,p)=0 \quad (2)$$

$$-\frac{\partial J_n}{\partial x}+G-U_n(n,p)=0 \quad (3)$$

$$J_p = q\mu_p - qD_p\frac{\partial p}{\partial x} \quad (4)$$

$$J_n = q\mu_n - qD_n\frac{\partial p}{\partial x} \quad (5)$$

Where (ψ) is the electrostatic potential, G and R are the generation and recombination rates, (J_n) and (J_p) denote the electron and hole current densities, and (N_D) and (N_A) represent donor and acceptor concentrations, respectively. The carrier transport equations are coupled and highly nonlinear; therefore, SCAPS-1D employs the Newton-Raphson iterative numerical method to solve the discretized semiconductor equations self-consistently. This method linearizes the nonlinear differential equations around an initial approximation and iteratively updates the solution until numerical convergence is achieved [10]. The Newton-Raphson algorithm ensures high computational stability and accuracy in calculating the electrostatic potential, carrier concentration profiles, electric field distribution, and current density across the device structure. The iterative correction procedure can be generally expressed as [10]:

$$x_{(n+1)} = x_{(n)} - \frac{f(x_n)}{f'(x_n)} \quad (6)$$

Where (x_n) is the current approximation, f (x_n) is the nonlinear function, and f' (x_n) is its derivative. The iterations continue until the variation between successive solutions becomes sufficiently small.

2.2. Device Architecture

The figure 01 showed the simulated solar cell structure, which consists of a multilayer heterojunction architecture arranged as: Fe/CuO/$Cs_2InSbCl_6$/CdS/TiO_2. In this configuration, (CuO) acts as the hole transport layer (HTL) due to its p-type conductivity and favorable valence band alignment, facilitating efficient hole extraction and transport toward the back contact. The ($Cs_2InSbCl_6$) double perovskite layer serves as the main photoactive absorber responsible for photon absorption and electron-hole pair generation. (CdS) was employed as the buffer layer because of its suitable conduction band alignment and ability to reduce interface recombination between the absorber and electron transport layer. (TiO_2) functions as the electron transport layer (ETL), ensuring efficient electron extraction and transport toward the front contact while blocking hole transport. The complete device architecture was constructed in SCAPS-1D with (Fe) as back metal contact attached to the (CuO) layer. It was defined with a work function of 4.8 eV. Its surface recombination velocity was set to 10^5 cm/s for electrons and 10^7 cm/s for holes, reflecting its role as a hole-collecting contact. The energy band alignment between the different layers promotes directional charge carrier separation, where photogenerated electrons are transported toward the (TiO_2) side and holes toward the (CuO) side, thereby minimizing recombination losses and enhancing photovoltaic performance. According to the figure 01, the absorber layer ($Cs_2InSbCl_6$) exhibits a strong absorption response within the visible region, indicating its excellent capability to harvest incident solar photons and generate electron-hole pairs efficiently. The high absorption coefficient in the short-wavelength region confirms the suitability of the perovskite material for photovoltaic applications. As the wavelength increases toward the near-infrared region, the absorption coefficient gradually decreases due to the reduction in photon energy relative to the absorber bandgap. Also, the inputs of each layer were tabulated in table 01 and 02.

Table 01. The simulated parameters of CuO, $Cs_2InSbCl_6$, CdS and TiO_2.

Parameters	CuO	$Cs_2InSbCl_6$	CdS	TiO_2
Thickness (µm)	0.2	500	0.04	0
Band gap (eV)	1.51	1.34	2.4	3.3
Electron affinity (eV)	4.07	4.1	4.2	4.5
Dielectric permittivity (relative)	18.1	5.5	10	09
CB effective density of states (cm-1)	5.6 E+17	2.1E+19	1.5E+18	2.20E+18
VB effective density of states (cm-1)	2.08 E+17	5.5E+19	1.8E+19	1.80E+19
Electron thermal velocity (cm/s)	1.0E+7	1.0E+7	1.0E+7	1.0E+7
Hole thermal velocity (cm/s)	1.0E+7	1.0E+7	1.0E+7	1.0E+7
Electron mobility	100	100	100	32
Hole mobility	20	0.1	25	3
Shallow uniform donor density ,N_D (cm^{-1})	0	1.0E+13	1.0E15	1.0E+19
Shallow uniform donor density ,N_A (cm^{-1})	1.0E+17	1.0E+13	0	0
References	[12],[23],[24]	[10]	[12]	[16],[3]

Table 02. The simulated parameters related to defects of CuO, $Cs_2InSbCl_6$, CdS and TiO_2.

PV parameters	CuO	$Cs_2InSbCl_6$	CdS	TiO_2
Defect density (Nt) (cm^{-3})	1.0E+14	1.0E+14	1.0E+14	1.0E+14
charge type	neutral	neutral	neutral	neutral
grading Nt (y)	uniform	uniform	uniform	uniform
energy distribution	single	single	single	single
Capture cross section electrons (cm^2)	1.000E-15	1.000E-15	1.000E-15	1.000E-15
Capture cross section holes (cm^2)	1.000E-15	1.000E-15	1.000E-15	1.000E-15
Tunnel mass	minimum	minimum	minimum	minimum
Interfaces defects CuO/ $Cs_2InSbCl_6$		1.0E+10		
Interfaces defects $Cs_2InSbCl_6/TiO_2$		1.0E+10		

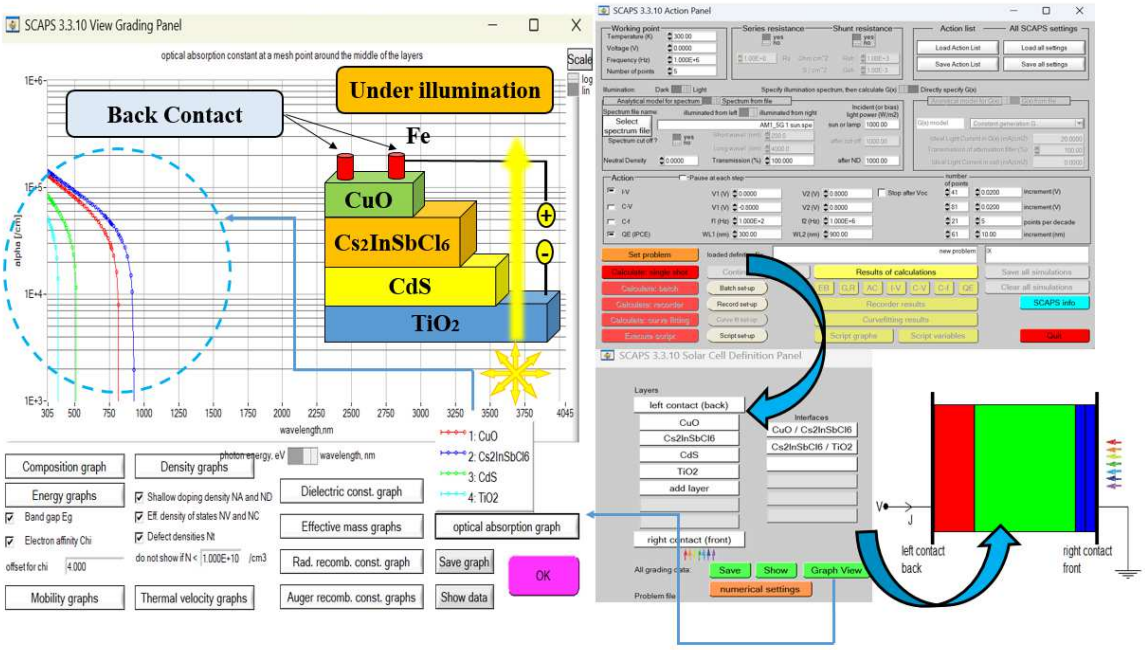


Figure 01. The simulated solar cell structure, multilayer heterojunction architecture Fe/CuO/$Cs_2InSbCl_6$/CdS/TiO_2.

2.3. Energy Band Diagram of $Cs_2InSbCl_6$

Figures 02 depict the energy band diagrams for three photovoltaic solar cells based on ($Cs_2InSbCl_6$), each utilizing a distinct ETL: (TiO_2). ETLs are essential in (PSCs) as they aid in the extraction of light-induced holes. For optimal electron transfer from the (ETL) to ($Cs_2InSbCl_6$) absorber, the ETL's ions must have greater energy than the absorber. In contrast, to ensure effective electron collection, the electron affinity of the (ETL) should be greater than that of ($Cs_2InSbCl_6$). Layer thickness is plotted along the x-axis (depth) in µm, while energy (in eV) is shown on the y-axis. Also the (HTL) layer is very essential to ensure the functionalization of our cell that's why the (CuO) was utilized as (HTL). Specially, the (CuO) has near work function to back contact (Fe). The quasi Fermi level illustrate the energy occupied charges carrier when illuminated and should be aligned between adjacent layers [3] as shown in figure 02. For the (ETL), the conduction band minimum (CBM) is higher than ($Cs_2InSbCl_6$)'s (CBM), facilitating the flow of electrons into the absorber [25]. Moreover, (TiO_2) has a near valence band maximum (VBM) to that of ($Cs_2InSbCl_6$), suggesting the good transport for electron [26].

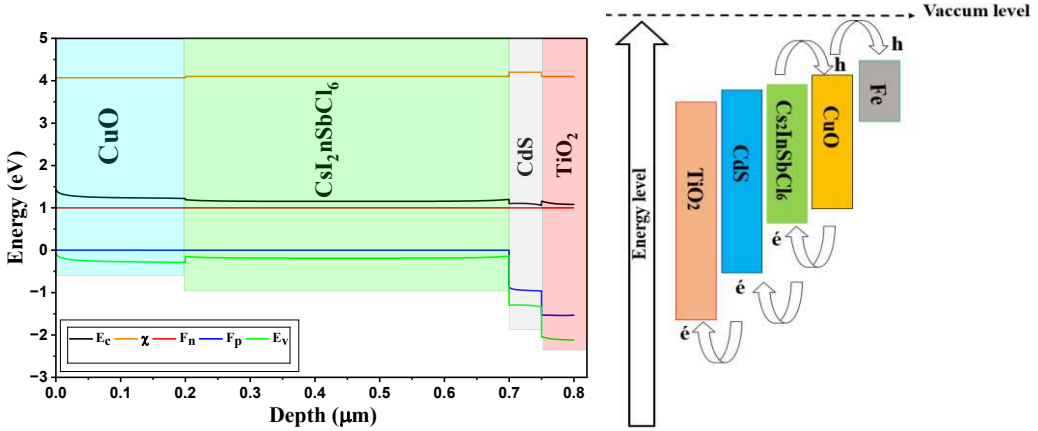


Figure 02. The diagram depicting the energy bands (in eV) of the solar cell structure.

3. Results and discussion:

3.1. Effect of thickness and bandgap energy of ($Cs_2InSbCl_6$).

The contour plots in figure 03 show the influence of the perovskite absorber thickness and bandgap energy (E_g) on the photovoltaic performance of your CuO/$Cs_2InSbCl_6$/CdS/TiO_2 solar cell. For the power conversion efficiency (PCE), the efficiency increases significantly as the absorber thickness rises from 0.2 to nearly 0.6-0.8 µm, mainly because a thicker absorber enhances photon absorption and generates more electron-hole pairs. The highest PCE values (~27.5 %) are obtained at intermediate bandgap energies around 1.25-1.35 eV. At larger bandgap values (>1.45 eV), the efficiency decreases because the absorber captures a smaller portion of the solar spectrum, leading to reduced photocurrent generation [27]. The short-circuit current density (J_{sc}) strongly depends on both thickness and (E_g). Lower bandgap energies produce higher (J_{sc}) values due to broader light absorption. Increasing the thickness from 0.2 to 1.0 µm also improves (J_{sc}), reaching values above (36 mA/cm^2). This behavior is associated with enhanced optical absorption and longer carrier generation paths inside the absorber layer [28]. The open-circuit voltage (V_{oc}) exhibits the opposite trend with respect to the bandgap. As (E_g) increases, (V_{oc}) rises because larger bandgap materials reduce intrinsic carrier concentration and suppress recombination losses [29]. The maximum (V_{oc}) approaches 1.0 V for high (E_g) values around 1.5-1.6 eV. However, excessive bandgap widening simultaneously lowers (Jsc), which limits the overall efficiency. The fill factor (FF) improves with increasing bandgap energy and remains relatively high over the investigated thickness range, with maximum values approaching 88 %. Higher (E_g) reduces recombination and improves carrier selectivity [30], leading to better diode quality and enhanced (FF). Overall, the results indicate that the optimal absorber parameters are obtained at a moderate bandgap of approximate ($E_g \approx$ 1.3 eV) and an absorber thickness near: (D ≈ 0.6-0.9 µm), where the balance between light absorption, carrier transport, and recombination yields the highest photovoltaic performance.

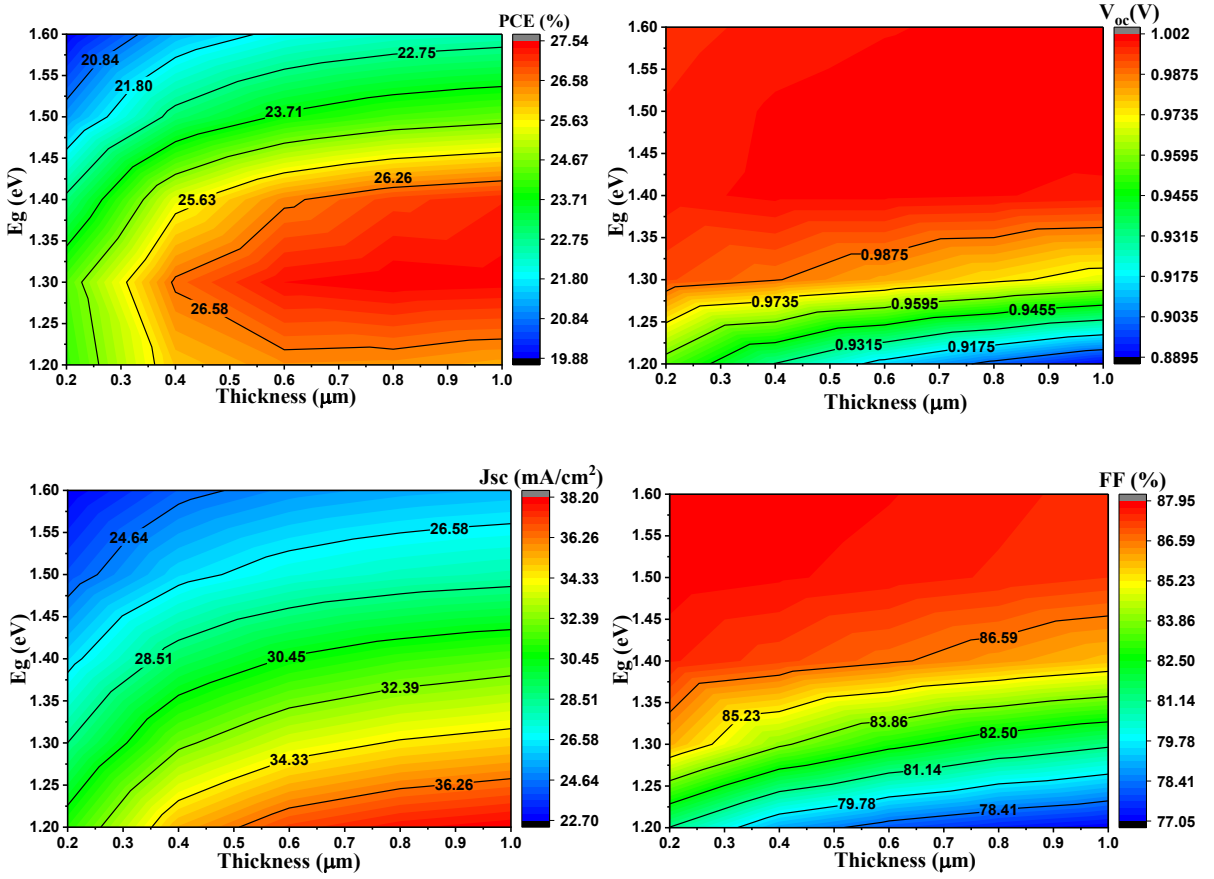


Figure 03. Contour diagrams illustrating the effect of thickness and bandgap of ($Cs_2InSbCl_6$) layer: (a) PCE, (b) V_{OC}, (c) J_{sc} and (d) FF.

3.2. Effect of thickness and bandgap energy of (CuO).

The figure 04 indicates that the (CuO) layer strongly influences charge extraction, interface recombination, and carrier transport inside the device. As the (CuO) thickness increases from approximately 0.02 µm to nearly 0.15-0.25 µm, the (PCE) improves significantly, reaching values close to 26-27 %. This enhancement is mainly attributed to improved hole collection efficiency and better interfacial contact between the absorber and (HTL). Thin (CuO) layers may lead to incomplete coverage and increased recombination losses, while moderate thicknesses provide efficient pathways for hole transport toward the (Fe) back contact [31]. However, when the (CuO) thickness exceeds nearly 0.3-0.4 µm, the device performance begins to decrease slightly due to increased series resistance and reduced carrier transport efficiency across the (HTL) layer (CuO) [32]. The (CuO) bandgap energy also has a pronounced influence on the solar cell characteristics. At lower bandgap energies around 1.2-1.3 eV, the device exhibits higher (J_{sc}), with values exceeding 35-36 mA/cm², because the (CuO) layer absorbs a larger portion of incident photons and facilitates hole extraction. Nevertheless, lower bandgap values increase recombination losses, which slightly reduce the (V_{oc}). As the (CuO) bandgap increases toward 1.5-1.6 eV, the (V_{oc}) rises progressively and approaches values around 0.95-1.0 V due to improved carrier selectivity and reduced recombination at the CuO/$Cs_2InSbCl_6$ interface. In addition, the (FF) increases from nearly 80 % to about 87-88 %, indicating improved diode quality and reduced resistive losses. However, excessively large (CuO) bandgap values may reduce carrier transport and slightly decrease the photocurrent density. Overall, the optimal photovoltaic performance is achieved for a (CuO) thickness in the range of approximately 0.15-0.25 µm and a bandgap energy close to 1.4-1.5 eV, where the balance between efficient hole extraction, minimized recombination, and low resistive losses results in maximum device efficiency. These results were aligned with previous researches [33].

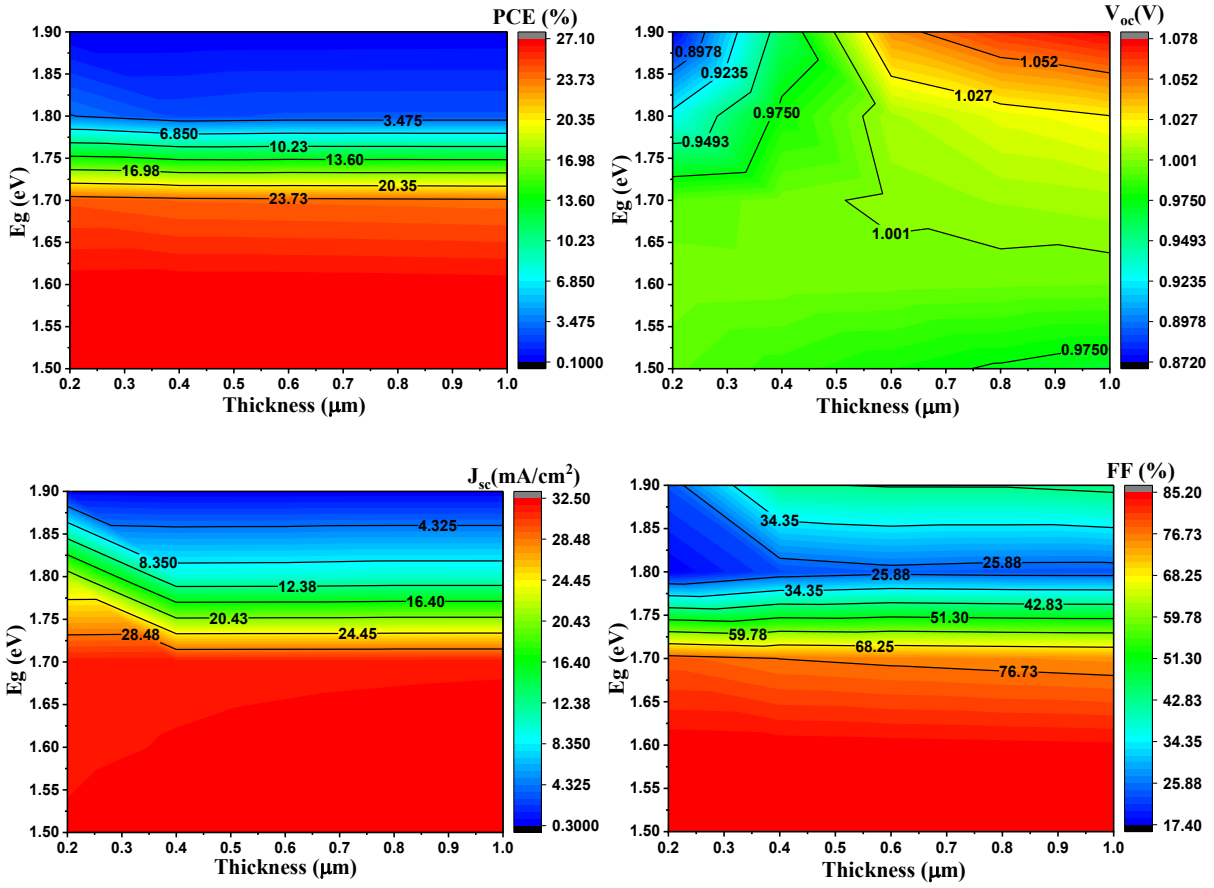


Figure 04. Contour diagrams illustrating the effect of thickness and bandgap of (CuO) layer: (a) PCE, (b) V_{OC}, (c) J_{sc} and (d) FF.

3.3. Effect of thickness and bandgap energy of (CdS).

The Figure 05 presents the influence of the (CdS) buffer layer thickness and bandgap energy on the photovoltaic performance of Fe/CuO/Cs2InSbCl6/CdS/TiO_2 solar cell. The (CdS) layer acts as a buffer layer between the ($Cs_2InSbCl_6$) absorber and the (TiO_2) electron transport layer. The obtained results reveal that the photovoltaic parameters exhibit only slight variations with changing (CdS) thickness and bandgap energy, indicating that the device performance is weakly sensitive to the CdS layer within the investigated range. As the (CdS) thickness increases from approximately 0.05 µm to 0.3 µm, the power conversion efficiency (PCE) remains nearly stable within the range of 27-27.6 %. This slight variation indicates that the (CdS) layer efficiently performs its role as a buffer layer without significantly affecting photon absorption or carrier transport [34]. Moderate CdS thicknesses provide sufficient interface coverage and minimize defect-assisted recombination at the absorber/ETL interface. The same observation were reported by Jenifer et al. [27]. The short-circuit current density (J_{sc}) also exhibits very small changes, remaining close to 31.8-31.9 mA/cm^2. This weak dependence originates from the relatively large bandgap energy of (CdS), which ensures high optical transparency in the visible region and minimizes parasitic absorption losses. Consequently, most incident photons successfully reach the absorber layer, preserving efficient photo carrier generation [35]. Similarly, the open-circuit voltage (V_{oc}) remains almost constant, varying only slightly between approximately 0.948 and 0.952 V. This behavior suggests that the (CdS) layer maintains stable band alignment and effective electron selectivity at the heterojunction interface, thereby limiting recombination losses. In addition, the fill factor (FF) remains relatively high and stable, fluctuating only from nearly 85.2 to 85.4 %. The optical behavior of (CdS) is mainly governed by its wide bandgap energy, typically ranging from 2.4 to 2.5 eV, which shifts its absorption edge toward shorter wavelengths and enhances visible-light transparency. Overall, the obtained results demonstrate that varying the (CdS) thickness and bandgap energy does not significantly affect the photovoltaic parameters of the proposed solar cell.

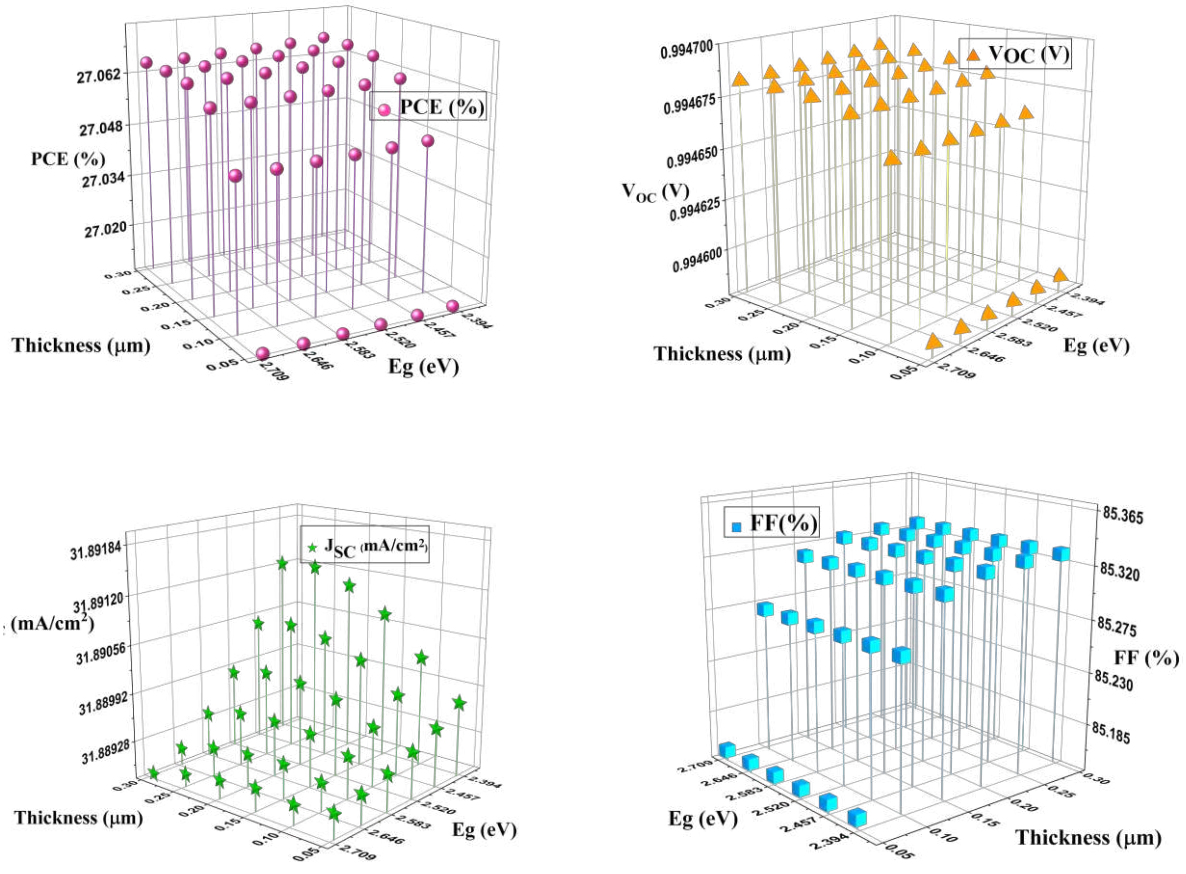


Figure 05. The effect of thickness and bandgap of (CdS) layer: (a) PCE, (b) V_{OC}, (c) J_{sc} and (d) FF.

3.4. Effect of thickness and bandgap energy of (TiO_2).

Figure 06 illustrates the influence of the (TiO_2) thickness and bandgap energy on the photovoltaic performance of oursolar cell. Compared with the absorber and (HTL) layers, the variation of (TiO_2) parameters produces relatively small changes in the photovoltaic characteristics, indicating that the device performance is less sensitive to the (ETL) properties within the investigated range. This behavior confirms the good electronic compatibility and stable band alignment of (TiO_2) with the CdS and the absorber layers. As the (TiO_2) thickness increases from approximately 0.05 to 0.3 µm, the power conversion efficiency (PCE) changes only slightly, remaining nearly within the range of 26.5-27.5 %. This weak variation indicates that (TiO_2) maintains efficient electron extraction even for different thickness values [36]. Similarly, the short-circuit current density (J_{sc}) exhibits only a small variation, fluctuating slightly between approximately 35 and 36 mA/cm^2. The weak dependence of (J_{sc})is mainly attributed to the large optical bandgap of (TiO_2), which minimizes parasitic absorption and allows most incident photons to reach the absorber layer independently of (ETL) thickness. The open-circuit voltage (V_{oc}) also remains relatively stable, varying only from nearly 0.94 to 0.99 V. Similar observations were reported in a previous study [37]. This slight improvement at higher (TiO_2) bandgap energies is associated with reduced interfacial recombination and improved electron selectivity at the ETL/absorber interface. In addition, the fill factor (FF) shows a slight variation of 0.005 %. The weak sensitivity of the photovoltaic parameters to (TiO_2) variations indicates that the (ETL) mainly acts as a stable electron-selective contact rather than an active light-absorbing layer. Due to its large bandgap energy 3.3 eV. Overall, the obtained results demonstrate that varying the (TiO_2) thickness and bandgap energy does not significantly alter the photovoltaic parameters of the proposed solar cell. This finding was deeply aligned with previous research [38].

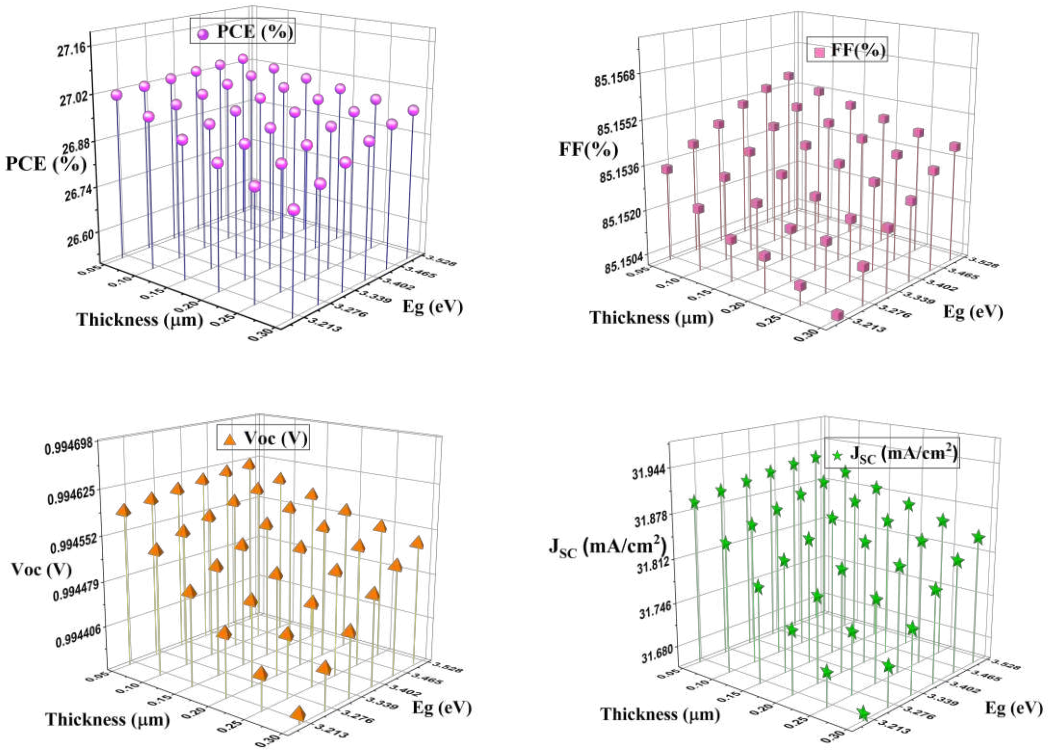


Figure 06. The effect of thickness and bandgap of (TiO_2) layer: (a) PCE, (b) V_{OC}, (c) J_{sc} and (d) FF.

3.5. Effect of temperature

The temperature-dependent characteristics of the Fe/CuO/$Cs_2InSbCl_6$/CdS/TiO_2 solar cell were investigated in the temperature range from 300 to 350 K in order to evaluate the thermal stability of the device. The obtained results in figure 07 demonstrate that temperature has a significant influence on the photovoltaic parameters due to its impact on carrier recombination, bandgap narrowing, and carrier transport mechanisms. As the temperature increases from 300 to 350 K, (V_{oc}) decreases noticeably from nearly 0.98 to about 0.72-0.75 V. This reduction is mainly attributed to the increase in intrinsic carrier concentration and enhanced recombination processes at elevated temperatures [39], which weaken the built-in electric field inside the device. In contrast, (J_{sc}) shows a slight increase with rising temperature, increasing from approximately 34-35 mA/cm² at 300 K to around 36-37 mA/cm² at 350 K. This behavior is associated with the reduction of the absorber bandgap at higher temperatures, allowing the absorption of a broader portion of the solar spectrum and generating more electron-hole pairs. However, the improvement in current density is not sufficient to compensate for the significant voltage losses. The (FF) also decreases gradually from nearly 87-88 % at 300 K to approximately 78-80 % at 350 K due to the increase in series resistance and thermally activated recombination effects. Consequently, the (PCE) decreases from about 27 % at room temperature to nearly 23 % at 350 K. The results indicate that the solar cell exhibits its best photovoltaic performance near standard test conditions (300 K), where the balance between carrier generation and recombination is optimized. At higher temperatures, thermal excitation enhances carrier scattering and defect-assisted recombination, leading to degradation in device efficiency [40]. Nevertheless, the relatively moderate reduction in (PCE) demonstrates that the CuO/$Cs_2InSbCl_6$/CdS/TiO_2 structure possesses acceptable thermal stability, making it a promising candidate for photovoltaic applications under varying environmental conditions.

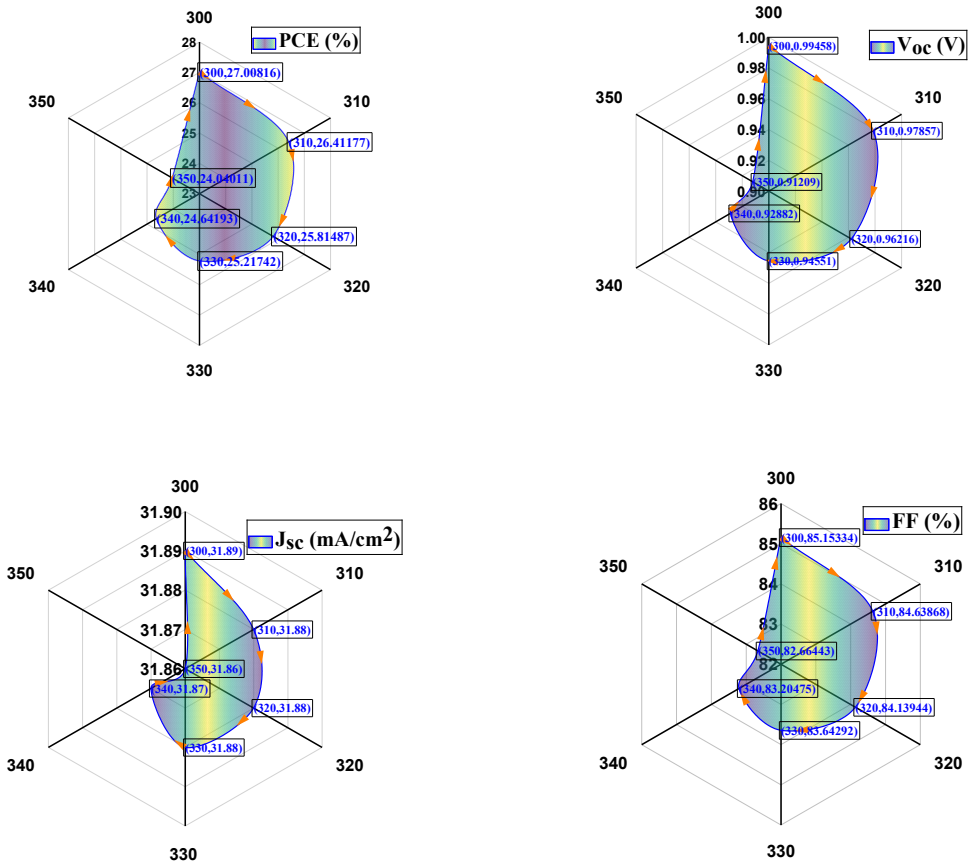


Figure 07. Plots illustrating the effect of temperature (300-350 K) on: PCE, V_{OC}, FF and Jsc.

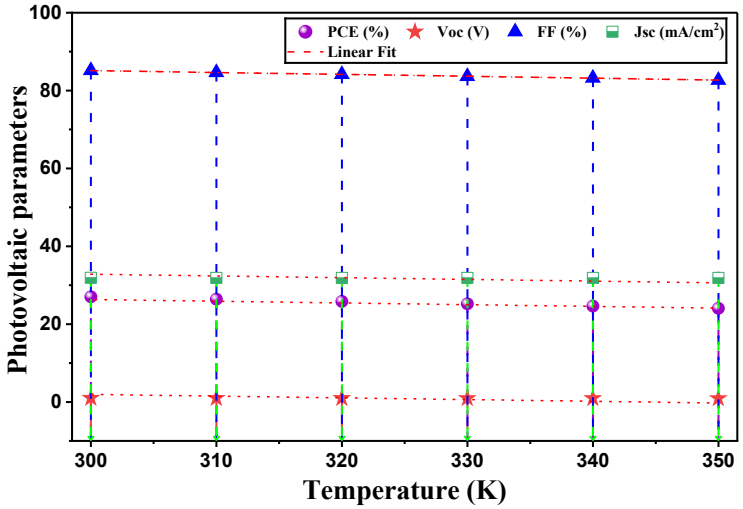


Figure 08. The fitted Plots illustrating the effect of temperature (300-350 K) on photovoltaic parameters.

The fitted profiles shown in figure 08 demonstrate an approximately linear deterioration of the photovoltaic parameters, namely the (PCE), (FF), (V_{oc}), and (J_{sc}), with increasing operating temperature. This thermal dependence is a critical issue in photovoltaic devices because solar cells in practical outdoor conditions are continuously exposed to temperature fluctuations that strongly influence carrier transport, recombination dynamics, and bandgap characteristics [41]. Therefore, evaluating the temperature coefficient (C_T) through the generalized linear relation is essential for predicting the operational reliability and thermal stability of the device under realistic environmental conditions [12]. Under standard test conditions (STC, 300 K), the temperature coefficients $C_{T\text{-}Y}$ (where Y corresponds to PCE, FF, Voc, and Jsc) quantitatively describe the sensitivity of each photovoltaic parameter to thermal variation. In this context, $PCE_{(STC)}$ denotes the conversion efficiency at STC, $FF_{(STC)}$ represents the fill factor, $V_{oc\,(STC)}$ corresponds to the open-circuit voltage, and $J_{sc\,(STC)}$ refers to the short-circuit current density measured at standard conditions. The $C_{T\text{-}Y}$ can be expressed as:

$$C_{T-Y} = \frac{1}{Y_{STC}} \times \frac{\Delta Y}{\Delta T} \times 100 \qquad (7)$$

Table 03. The variation of temperature coefficient between 300 and 350 K.

PV parameters	Unit	$\Delta Y/\Delta T$	Unit	C_T	Unit
PCE	(%)	-0.06	(%.K^{-1})	-0.22	(%.K^{-1})
FF (%)	(%)	0.05	(%.K^{-1})	-0.06	(%.K^{-1})
V_{oc}	(V)	0.0017	(mV.K^{-1})	-0.17	(mV.K^{-1})
J_{sc}	(mA/cm^2)	0.0005	(mA/cm^2.K)	-0.016	(mA/cm^2.K)

The simulated results in table 03 reveal that the investigated solar cell exhibits an efficiency temperature coefficient of -0.22 % K^{-1}, accompanied by a V_{oc} degradation rate of -0.17 mV.K^{-1} and a fill factor reduction of -0.06 % K^{-1}. The decrease in efficiency with increasing temperature can mainly be attributed to enhanced carrier recombination processes and the thermally induced narrowing of the semiconductor bandgap. As temperature rises, the intrinsic carrier concentration increases significantly, leading to stronger Shockley-Read-Hall (SRH) recombination and higher reverse saturation current density [42]. Consequently, the balance between photogenerated carrier collection and recombination becomes unfavorable, resulting in reduced photovoltaic conversion efficiency. Among all photovoltaic parameters, (V_{oc}) is the most temperature-sensitive parameter due to its logarithmic dependence on the saturation current density. The observed reduction of 0.17 mV.K^{-1} is consistent with reported values for high-performance perovskite and oxide-based solar cells, confirming the physical reliability

of the simulation results. The decrease in (V_{oc}) originates from the exponential increase in dark saturation current caused by thermally activated carrier recombination and defect-assisted transport mechanisms. Furthermore, elevated temperature enhances phonon scattering and interface recombination, which weakens the quasi-Fermi level splitting and consequently reduces (V_{oc}) [12].

The fill factor also decreases gradually with temperature because of the combined effects of increased series resistance, enhanced carrier scattering, and reduced carrier mobility at elevated temperatures. Thermal agitation deteriorates charge transport across the interfaces and promotes resistive losses. However, the relatively small FF degradation coefficient (-0.06 % K^{-1}) indicates that the device maintains acceptable charge extraction capability even under thermal stress. In contrast, Jsc exhibits only minor variation with increasing temperature, indicating that the photogeneration process remains relatively stable. This weak temperature dependence can be explained by the slight enhancement in photon absorption resulting from bandgap narrowing, which partially compensates for thermally induced recombination losses [17]. Therefore, the current generation capability of the solar cell is less affected compared to (V_{oc}) and (FF). Overall, the obtained thermal coefficients demonstrate that the proposed solar cell possesses moderate thermal stability and acceptable operational robustness under elevated-temperature conditions. Although the gradual efficiency degradation indicates some thermal sensitivity, the relatively low Voc loss and stable Jsc behavior suggest that the device can operate efficiently in hot climates without severe electrical performance deterioration. These findings confirm the suitability of the investigated architecture for photovoltaic applications in regions characterized by high solar irradiance and elevated ambient temperatures [43].

4. Optimized solar cell.

Figure (8.a) presents the external quantum efficiency (QE) spectra before and after optimization over the wavelength range of 300-900 nm. The optimized device demonstrates significantly enhanced spectral response, particularly in the short- and long-wavelength regions. In the short-wavelength region (300-400nm), the improvement is mainly attributed to better carrier extraction and reduced parasitic absorption losses within the transport layers. In the visible region, the QE remains close to 100 %, confirming efficient photon absorption and excellent carrier collection capability inside the ($Cs_2InSbCl_6$) absorber layer. Moreover, the optimized structure exhibits a delayed (QE) drop in the long-wavelength region near 800-900 nm, indicating enhanced absorption of low-energy photons due to improved absorber thickness optimization and favorable bandgap alignment. In figure (8.b) the spectral response (SR) elevated from 0.58 to 0.65 A/W. Figure (8.c) presents the illuminated current density-voltage (J-V) characteristics of the optimized and non-optimized solar cell. The results reveal a noticeable enhancement in photovoltaic performance after optimization. The optimized device exhibits an increase in power conversion efficiency from nearly 26.35 %before optimization to approximately 28 % after optimization, accompanied by improvements in fill factor and current extraction capability. The optimized structure also demonstrates a more stable current plateau under reverse bias conditions and reduced current degradation near the open-circuit voltage region, indicating suppression of recombination losses and improved carrier transport dynamics. The enhancement mainly originates from better absorber thickness and bandgap optimization, which improved optical absorption and carrier collection efficiency while minimizing leakage current across the heterojunction interfaces. The equation was utilized to determine the ideality factor (n) [44]:

$$J = J_0\left(e^{\frac{qV}{nKT}} - 1\right) \tag{8}$$

$$J \approx J_0\left(e^{\frac{qV}{nKT}}\right) \tag{9}$$

$$\ln(J) = \frac{qV}{nKT} + \ln(J_0) \tag{10}$$

The inset of figure (8.c) illustrates the linear fitting of the ln (J) versus (V) characteristics used to determine the diode ideality factor. The slope increased from approximately 21.95 before optimization to nearly 23.64 after optimization, resulting in a reduction of the ideality factor from approximately 1.8 to nearly 1.6. This reduction confirms a significant suppression of trap-assisted Shockley-Read-Hall recombination and improved diode quality after optimization. The lower ideality factor further indicates that the carrier transport mechanism shifted closer to an ideal diffusion-dominated regime due to reduced interface defect density and enhanced band alignment between adjacent layers. The Nyquist plot in figure (8.d) shows a decreasing in semi-circle after the optimization which confirms the minimization of recombination process. To evaluate our findings with the previous studies, our Fe/CuO/$Cs_2InSbCl_6$/CdS/TiO_2 solar cells was compared in table 04 which showed attractive results.

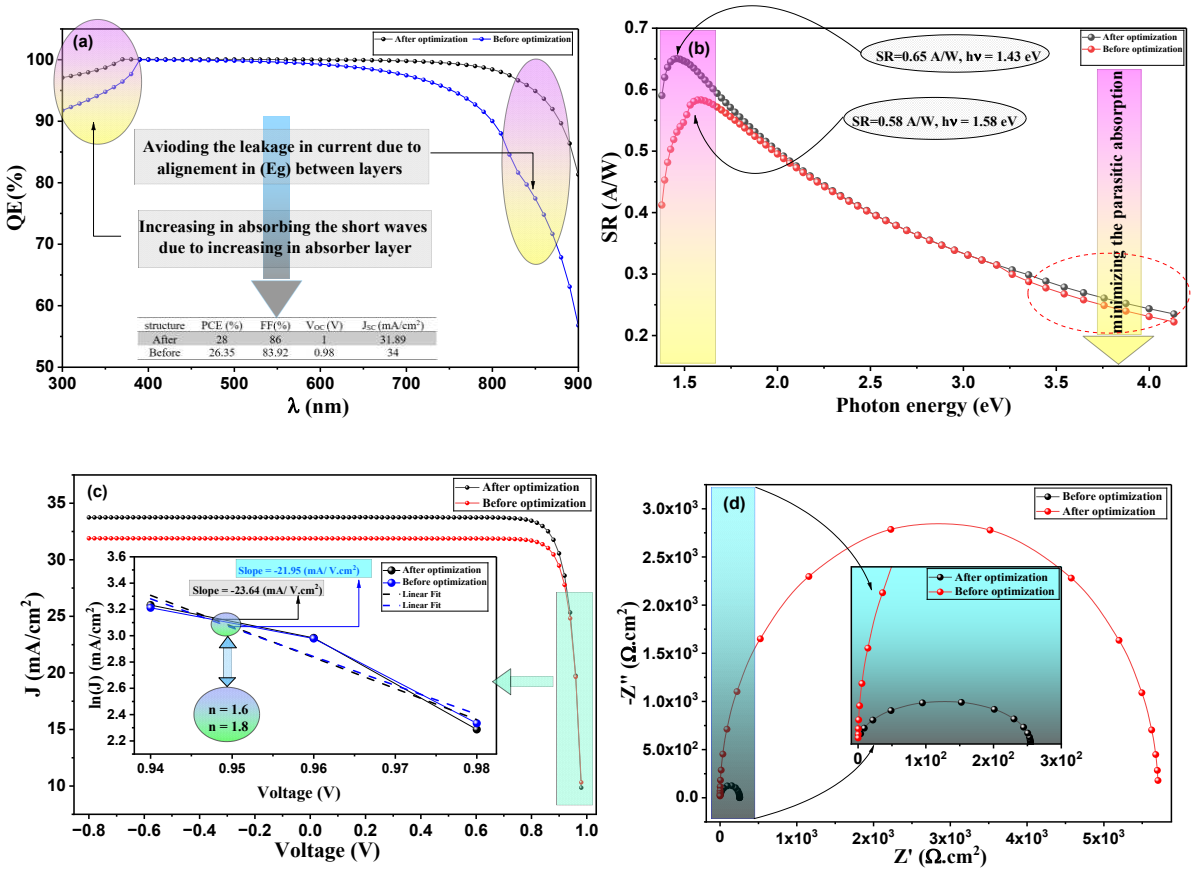


Figure 08. The (QE), (SR), (J-V) and Nyquist plot for Fe/CuO/$Cs_2InSbCl_6$/CdS/TiO_2 solar cell after and before the optimization.

Table 04. Comparative table with the previous studies.

Structure	PCE (%)	References
LBSO/Cs_2TiBr_6/CNTS	24.82	[45]
PEDOT: PSS/ Cs_2TiBr6/TiO_2	17.83	[46]
SnO_2/Cs_2BiAgI_6/CBTS/Au	21.52	[40]
TiO_2/$Cs_2InSbCl_6$/Cu2O	20.71	[10]
Ni/CuO/Cs_2SnBr_6/CdS/FTO	23.25	[4]
ZnO /CH3NH3Snl3/ Spiro-OMeTAD/Au	24	[8]
ITO/Spiro-OMeTAD/$Cs_2AgBiBr_6$/SnO_2/Au	26.3	[5]
Cu_2O/$BaZrS_3$/TiO_2/FTO	18.85%	[19]
Ni/SnS/Cu_2SnSe_3/TiO_2/ITO/Al	27	[17]
Fe/CuO/$Cs_2InSbCl_6$/CdS/TiO_2	28	The present work

Funding declaration

This research did not receive any specific grant from funding agencies in the public, commercial, or not-for-profit sectors.

Data availability

All data that support the findings of this study are included within this article.

Conflicts of interest

There are no conflicts to declare.

Conclusion

In this work, a high-performance Fe/CuO/$Cs_2InSbCl_6$/CdS/TiO_2 heterostructure solar cell was numerically investigated using the SCAPS-1D simulator in order to evaluate the influence of layer thickness, bandgap energy, and operating temperature on the photovoltaic performance of the device under AM1.5G illumination conditions. The optical absorption analysis demonstrated that the ($Cs_2InSbCl_6$) absorber layer exhibits strong absorption within the visible spectral region, ensuring efficient photon harvesting and enhanced photogenerated carrier density. In contrast, the (CdS) and (TiO_2) layers maintained high optical transparency due to their wide bandgap energies, thereby minimizing parasitic absorption losses and improving light transmission toward the absorber layer. The optimization study revealed that the photovoltaic performance strongly depends on the absorber layer properties. Increasing the absorber thickness significantly enhanced the light absorption capability and carrier generation rate, leading to improved photovoltaic parameters. However, excessively large thicknesses increased carrier transport distance and recombination probability. The optimal photovoltaic response was achieved for absorber thicknesses close to 0.9 μm and bandgap energy around 1.4 eV. The (CuO) hole transport layer exhibited a more pronounced influence on the device performance compared with the (CdS) and (TiO_2) layers due to its direct role in hole extraction and interface recombination control. In contrast, variations in the (CdS) buffer layer and (TiO_2) electron transport layer produced only slight changes in the photovoltaic parameters, confirming the good electronic compatibility and stable band alignment of these layers with the ($Cs_2InSbCl_6$). The thermal stability analysis revealed that increasing temperature from 300 to 350 K leads to gradual degradation of the photovoltaic parameters due to enhanced carrier recombination, increased saturation current density, and thermally induced bandgap narrowing. The (V_{oc}) was identified as the most temperature-sensitive parameter, while the J_{SC} (mA/cm^2) exhibited relatively weak thermal dependence. Despite the observed efficiency reduction from 27 to 24 %, the proposed device maintained acceptable thermal stability under elevated-temperature conditions. Under optimized conditions, the proposed solar cell achieved a high photovoltaic performance with power conversion efficiency approaching nearly 28 %, accompanied by high fill factor (86 %) and stable current density characteristics. These

results confirm that the Fe/CuO/$Cs_2InSbCl_6$/CdS/TiO_2 architecture represents a promising candidate for next-generation perovskite-based photovoltaic applications owing to its favorable band alignment, efficient carrier extraction, strong optical absorption, and acceptable thermal stability.

Mouad Chettab

Ph.D. student in Physics at Brothers Mentouri University of Constantine, Algeria, with a research focus on inorganic synthesis, thin films, and interface engineering within the Thin Films and Interfaces Research Laboratory. Experienced in the fabrication and characterization of metal oxide thin films using techniques such as spray pyrolysis, as well as in numerical simulation of solar cells using SCAPS-1D. Holds a Master's degree in Physics (2020), where his work centered on the optimization of photovoltaic device performance through material and structural engineering. MY current research interests include the development of advanced functional materials for photovoltaic and optoelectronic applications, with particular emphasis on doping strategies, defect control, and interface optimization.

References

[1] B. Rezini *et al.*, "Exploring the Optoelectronic Properties and Solar Cell Performance of Cs2SnI6−xBrx Lead-Free Double Perovskites: Combined DFT and SCAPS Simulation," *Physics*, vol. 7, no. 1, p. 3, Jan. 2025, doi: 10.3390/physics7010003.

[2] M. I. Hossain, P. Chelvanathan, A. Khandakar, K. Thomas, A. Rahman, and S. Mansour, "Enhanced efficiency of bifacial perovskite solar cells using computational study," *Sci. Rep.*, vol. 14, no. 1, p. 12984, Jun. 2024, doi: 10.1038/s41598-024-62487-0.

[3] M. Noman, A. H. H. Khan, and S. T. Jan, "Interface engineering and defect passivation for enhanced hole extraction, ion migration, and optimal charge dynamics in both lead-based and lead-free perovskite solar cells," *Sci. Rep.*, vol. 14, no. 1, p. 5449, Mar. 2024, doi: 10.1038/s41598-024-56246-4.

[4] Md. S. Reza *et al.*, "High-efficiency and eco-friendly Cs_2 $SnBr_6$ -based perovskite solar cells: optimized device architecture and performance analysis via SCAPS-1D simulation," *Opt. Express*, vol. 33, no. 14, p. 30441, Jul. 2025, doi: 10.1364/OE.566116.

[5] H. Sabbah, Z. Abdel Baki, R. Mezher, and J. Arayro, "SCAPS-1D Modeling of Hydrogenated Lead-Free Cs2AgBiBr6 Double Perovskite Solar Cells with a Remarkable Efficiency of 26.3%," *Nanomaterials*, vol. 14, no. 1, p. 48, Dec. 2023, doi: 10.3390/nano14010048.

[6] J. Al Mahmud *et al.*, "Design and analysis of a SnS_2 /WS_2 /V_2 O_5 double-heterojunction toward high-performance photovoltaics," *Energy Adv.*, vol. 2, no. 11, pp. 1843–1858, 2023, doi: 10.1039/D3YA00231D.

[7] T. THOMAS, "Simulation Study of Cs2TiBr6 Perovskite Solar Cells Using Graphene Oxide as a Novel HTL Layer Using SCAPS 1-D," *Renew. Energy Res. Appl.*, no. Online First, Dec. 2022, doi: 10.22044/rera.2022.12175.1154.

[8] S. Rabhi, H. Benzouid, A. Slami, and K. Dadda, "Modeling and Numerical Simulation of a CH3NH3SnI3 Perovskite Solar Cell Using the SCAPS1-D Simulator," in *ASEC 2023*, MDPI, Oct. 2023, p. 97. doi: 10.3390/ASEC2023-15300.

[9] Md. Tarekuzzaman and K. I. F. Utsho, "Advancing Solar Energy with Cs_2 $TlAsI_6$ Double Halide Perovskite: A Simulation-Driven Approach for High-Efficiency Solar Cell," *Adv. Electron. Mater.*, vol. 11, no. 16, p. e00312, Oct. 2025, doi: 10.1002/aelm.202500312.

[10] G. A. Nowsherwan, "Performance engineering of Cs2InSbCl6 lead-free double perovskite solar cells: insights from DFT, SCAPS-1D, wxAMPS, AFORS-HET, Oghmanano, and COMSOL," *Discov. Mater.*, vol. 6, no. 1, p. 15, Dec. 2025, doi: 10.1007/s43939-025-00466-6.

[11] M. K. Hossain *et al.*, "Deep Insights into the Coupled Optoelectronic and Photovoltaic Analysis of Lead-Free $CsSnI_3$ Perovskite-Based Solar Cell Using DFT Calculations and SCAPS-1D Simulations," *ACS Omega*, vol. 8, no. 25, pp. 22466–22485, Jun. 2023, doi: 10.1021/acsomega.3c00306.

[12] M. Chettab *et al.*, "Influence of Physical Parameters on p-CuO/n-CdS/n-Zn2SnO4 Solar cell: A Numerical Investigation Achieving Efficiency of 28.50 % Using SCAPS-1D," 2026.

[13] M. Abdelfatah, A. M. El Sayed, W. Ismail, S. Ulrich, V. Sittinger, and A. El-Shaer, "SCAPS simulation of novel inorganic ZrS2/CuO heterojunction solar cells," *Sci. Rep.*, vol. 13, no. 1, p. 4553, Mar. 2023, doi: 10.1038/s41598-023-31553-4.

[14] L. A. Lotfy, M. Abdelfatah, S. W. Sharshir, A. A. El-Naggar, W. Ismail, and A. El-Shaer, "Numerical simulation and optimization of FTO/TiO2/CZTS/CuO/Au solar cell using SCAPS-1D," *Sci. Rep.*, vol. 15, no. 1, p. 28022, Jul. 2025, doi: 10.1038/s41598-025-12999-0.

[15] A. Rahal *et al.*, "Optimization of structural and electronic properties in CuO/CIGS hybrid solar cells for high-efficiency, sustainable energy conversion," *RSC Adv.*, vol. 15, no. 29, pp. 23311–23318, 2025, doi: 10.1039/D5RA04283F.

[16] M. Rahaman, M. Hasan, R. Md. Moinuddin, and Md. N. Islam, "Numerical optimization of lead-based and lead-free absorber materials for perovskite solar cell (PSC) architectures: A SCAPS-1D simulation," *AIP Adv.*, vol. 14, no. 9, p. 095019, Sep. 2024, doi: 10.1063/5.0217486.

[17] M. Rahman, "Design and simulation of a high-performance Cd-free Cu2SnSe3 solar cells with SnS electron-blocking hole transport layer and TiO2 electron transport layer by SCAPS-1D," *SN Appl. Sci.*, vol. 3, Feb. 2021, doi: 10.1007/s42452-021-04267-3.

[18] B. Islam, T. M. Khan, Md. M. Rahaman, and S. R. A. Ahmed, "Computational optimization of $MASnI_3$ perovskite solar cells using SCAPS-1D simulations and machine learning techniques," *RSC Adv.*, vol. 16, no. 2, pp. 1172–1192, 2026, doi: 10.1039/D5RA07200J.

[19] S. Karthick, S. Velumani, and J. Bouclé, "Chalcogenide BaZrS3 perovskite solar cells: A numerical simulation and analysis using SCAPS-1D," *Opt. Mater.*, vol. 126, p. 112250, Apr. 2022, doi: 10.1016/j.optmat.2022.112250.

[20] M. Burgelman, P. Nollet, and S. Degrave, "Modelling polycrystalline semiconductor solar cells," *Thin Solid Films*, vol. 361–362, pp. 527–532, Feb. 2000, doi: 10.1016/S0040-6090(99)00825-1.

[21] M. U. Salman *et al.*, "Direct correlation between open-circuit voltage and quasi-fermi level splitting in perovskite solar cells: a computational step involving thickness, doping, lifetime, and temperature variations for green solutions," *RSC Adv.*, vol. 15, no. 20, pp. 15618–15629, 2025, doi: 10.1039/D5RA01868D.

[22] J. C. Z. Medina *et al.*, "Numerical Simulation and Performance Optimization of a Solar Cell Based on WO3/CdTe Heterostructure Using NiO as HTL Layer by SCAPS 1D," *Coatings*, vol. 13, no. 8, p. 1436, Aug. 2023, doi: 10.3390/coatings13081436.

[23] M. R. Kabir *et al.*, "A comprehensive SCAPS-1D simulation study on the photovoltaic properties and efficiency enhancement of CH_3 NH_3 $PbCl_3$ perovskite solar cells," *Eng. Res. Express*, vol. 7, no. 1, p. 015319, Mar. 2025, doi: 10.1088/2631-8695/ada721.

[24] M. Chettab *et al.*, "Eco-Bifunctional CuO Thin films: Tuning antibacterial and photocatalytic response via molarity adjustment molarities using spray pyrolysis," May 13, 2026, *In Review*. doi: 10.21203/rs.3.rs-9581586/v1.

[25] S. Mehmood, Y. Xia, F. Qu, and M. He, "Investigating the Performance of Efficient and Stable Planer Perovskite Solar Cell with an Effective Inorganic Carrier Transport Layer Using SCAPS-1D Simulation," *Energies*, vol. 16, no. 21, p. 7438, Nov. 2023, doi: 10.3390/en16217438.

[26] R. Ranjan *et al.*, "SCAPS study on the effect of various hole transport layer on highly efficient 31.86% eco-friendly CZTS based solar cell," *Sci. Rep.*, vol. 13, Oct. 2023, doi: 10.1038/s41598-023-44845-6.

[27] K. Jenifer, B. Gururajan, W. Liu, and S. Parthiban, "Numerical Investigation of Eco-Friendly All-Zinc Based Thin Film Solar Cells For Sustainable Photovoltaics," *Adv. Theory Simul.*, vol. 8, no. 11, p. e00157, Nov. 2025, doi: 10.1002/adts.202500157.

[28] F. Belarbi, W. Rahal, D. Rached, S. Benghabrit, and M. Adnane, "A comparative study of different buffer layers for CZTS solar cell using Scaps-1D simulation program," *Optik*, vol. 216, p. 164743, Aug. 2020, doi: 10.1016/j.ijleo.2020.164743.

[29] M. Atowar Rahman, "Enhancing the photovoltaic performance of Cd-free Cu2ZnSnS4 heterojunction solar cells using SnS HTL and TiO2 ETL," *Sol. Energy*, vol. 215, pp. 64–76, Feb. 2021, doi: 10.1016/j.solener.2020.12.020.

[30] M. U. Salman and S. Atiq, “Analysis of short-circuit current suppression mediated by strategically optimized buffer layer thickness in heterojunction solar cells,” *Energy Adv.*, vol. 4, no. 12, pp. 1500–1509, 2025, doi: 10.1039/D5YA00290G.

[31] A. Shrivastava, S. Saini, D. Kumari, S. Singh, and J. Adam, “Quantum-to-classical modeling of monolayer Ge_2 Se_2 and its application in photovoltaic devices,” *Beilstein J. Nanotechnol.*, vol. 15, pp. 1153–1169, Sep. 2024, doi: 10.3762/bjnano.15.94.

[32] H. Sabbah, Z. Abdel Baki, R. Mezher, and J. Arayro, “SCAPS-1D Modeling of Hydrogenated Lead-Free Cs2AgBiBr6 Double Perovskite Solar Cells with a Remarkable Efficiency of 26.3%,” *Nanomaterials*, vol. 14, no. 1, p. 48, Dec. 2023, doi: 10.3390/nano14010048.

[33] K. I. Ferdous Utsho *et al.*, “Optimizing Cs_2 $CuBiBr_6$ double halide perovskite for solar applications: the role of electron transport layers in SCAPS-1D simulations,” *RSC Adv.*, vol. 15, no. 3, pp. 2184–2204, 2025, doi: 10.1039/D4RA08515A.

[34] T. A. Chowdhury, “Numerical modeling to enhance the efficiency of experimentally fabricated Sb_2 Se_3 -based solar cell,” *RSC Adv.*, vol. 16, no. 3, pp. 2873–2903, 2026, doi: 10.1039/D5RA04411A.

[35] K. Sarker, Md. S. Sumon, Mst. F. Orthe, S. K. Biswas, and Md. M. Ahmed, “Numerical Simulation of High Efficiency Environment Friendly CuBi2O4-Based Thin-Film Solar Cell Using SCAPS-1D,” *Int. J. Photoenergy*, vol. 2023, pp. 1–11, Apr. 2023, doi: 10.1155/2023/7208502.

[36] F. Saidi, I. Bouchama, M. Merabet, M. Hadjab, S. Rabhi, and M. Chettab, “Optimization of different ETL and BSF Layers with defects Management for high-performance CIGS solar cells,” 2026.

[37] H.-J. Park, H. Son, and B.-S. Jeong, “SCAPS-1D Simulation for Device Optimization to Improve Efficiency in Lead-Free CsSnI3 Perovskite Solar Cells,” *Inorganics*, vol. 12, no. 4, p. 123, Apr. 2024, doi: 10.3390/inorganics12040123.

[38] L. A. Lotfy, M. Abdelfatah, S. W. Sharshir, A. A. El-Naggar, W. Ismail, and A. El-Shaer, “Numerical simulation and optimization of FTO/TiO2/CZTS/CuO/Au solar cell using SCAPS-1D,” *Sci. Rep.*, vol. 15, no. 1, p. 28022, Jul. 2025, doi: 10.1038/s41598-025-12999-0.

[39] P. Afrin, K. Farjana, A. Vumije, and Md. N. Uddin, “An investigation on the impact of temperature variation over the performance of formamidinium tin iodide perovskite solar cell using SCAPS simulation,” *AIP Adv.*, vol. 14, no. 7, p. 075123, Jul. 2024, doi: 10.1063/5.0209332.

[40] M. K. Hossain *et al.*, “Combined DFT, SCAPS-1D, and wxAMPS frameworks for design optimization of efficient Cs_2 $BiAgI_6$ -based perovskite solar cells with different charge transport layers,” *RSC Adv.*, vol. 12, no. 54, pp. 34850–34873, 2022, doi: 10.1039/D2RA06734J.

[41] A. C. Ozurumba *et al.*, “SCAPS-1D simulated organometallic halide perovskites: A comparison of performance under Sub-Saharan temperature condition,” *Heliyon*, vol. 10, no. 8, p. e29599, Apr. 2024, doi: 10.1016/j.heliyon.2024.e29599.

[42] T. M. Khan, B. Islam, and S. R. A. Ahmed, “Performance analysis and optimization of SnSe thin-film solar cell with Cu2O HTL through a combination of SCAPS-1D and machine learning approaches”.

[43] S. Bhandari, A. Roy, A. Ghosh, T. K. Mallick, and S. Sundaram, “Perceiving the temperature coefficients of carbon-based perovskite solar cells,” *Sustain. Energy Fuels*, vol. 4, no. 12, pp. 6283–6298, 2020, doi: 10.1039/D0SE00782J.

[44] S. H. Zyoud *et al.*, “Numerical Modeling of High Conversion Efficiency FTO/ZnO/CdS/CZTS/MO Thin Film-Based Solar Cells: Using SCAPS-1D Software,” *Crystals*, vol. 11, no. 12, p. 1468, Nov. 2021, doi: 10.3390/cryst11121468.

[45] M. K. Hossain *et al.*, “Exploring the Optoelectronic and Photovoltaic Characteristics of Lead-Free Cs_2 $TiBr_6$ Double Perovskite Solar Cells: A DFT and SCAPS-1D Investigations,” *Adv. Electron. Mater.*, vol. 11, no. 2, p. 2400348, Feb. 2025, doi: 10.1002/aelm.202400348.

[46] S. A. Moiz, A. N. M. Alahmadi, and A. J. Aljohani, “Design of a Novel Lead-Free Perovskite Solar Cell for 17.83% Efficiency,” *IEEE Access*, vol. 9, pp. 54254–54263, 2021, doi: 10.1109/ACCESS.2021.3070112.